Unveiling the impact of the effective particles distribution on strengthening mechanisms: A multiscale characterization of Mg+Y2O3 nanocomposites

C. Mallmann, F. Hannard, E. Ferrie, A. Simar, R. Daudin, P. Lhuissier, A. Pacureanu, Fivel Marc

Unveiling the impact of the effective particles distribution on strengthening mechanisms: a multiscale characterization of Mg+Y_2O_3 nanocomposites

C. Mallmann[a], F. Hannard[b], E. Ferrié[a], A. Simar[b], R. Daudin[a], P. Lhuissier[a], A. Pacureanu[c], M. Fivel[a]

[a] *University of Grenoble Alpes, CNRS, SIMaP, 38000 Grenoble, France*
[b] *UCLouvain-iMMC-IMAP, Place Sainte Barbe 2, B1348, Louvain-la-Neuve Belgium*
[c] *European Synchrotron Radiation Facility (ESRF), 71 Avenue des Martyrs, 38000 Grenoble, France*

Abstract

Most models used to account for the hardening of nanocomposites only consider a global volume fraction of particles which is a simplified indicator that overlooks the particles size and spatial distribution. The current study aims at quantifying the effect of the real experimental particles spatial and size distribution on the strengthening of a magnesium based nanocomposites reinforced with Y_2O_3 particles processed by Friction Stir Processing (FSP). X-ray tomographic 3-D images allowed to identify the best FSP parameters for the optimum nanocomposite. A detailed analysis indicates that the observed hardening is mainly due to Orowan strengthening and the generation of geometrically necessary dislocations (GND) due to thermal expansion coefficients (CTE) mismatch between magnesium and Y_2O_3 particles. A multiscale characterization coupling 3D X-ray laboratory, synchrotron nanoholotomography and transmission electron microscopy (TEM) has been used to investigate particles size and spatial distribution over four orders of magnitude in length scales. Two dedicated micromechanical models for the two strengthening mechanisms are applied on the experimental particle fields taking into account the real particles size and spatial distribution, and compared to classical models based on average data. This required to develop a micromechanical model for CTE mismatch hardening contribution. This analysis reveals that the contribution from CTE mismatch is decreased by a factor two when taking into account the real distribution of particles instead of an average volume fraction.

Keywords: Magnesium, nanocomposite, Friction Stir Processing (FSP), tomography, strengthening mechanisms

1. Introduction

Magnesium based nanocomposites have attracted much attention over the past few years [1] as a promising solution to light weighting, energy saving and emission reduction, especially for automotive and aerospace applications. This is due to magnesium's low specific weight (1.74 g.cm^{-3}), which gives it a huge potential to be used in applications that require lightweighting. The addition of a low volume fraction of nanoreinforcements results in the improvement of mechanical properties without compromising the density, but a homogeneous dispersion of the reinforcement particles is needed in order to achieve a strengthening effect [2, 3, 4, 5, 6].

Dispersion of the reinforcements is hence one of the main issues of concern in the processing of magnesium based composites, together with the quality of the reinforcement/matrix interface. Small particles, especially nanoparticles due to their high surface to volume ratio, tend to agglomerate and form clusters which are difficult to break, leading to an inhomogeneous distribution of particles within the matrix. Several liquid and solid processing routes have been developed to elaborate nanocomposites. Considering liquid phase techniques, Erman *et al.* [2], Wang *et al.* [7] and Chen *et al.* [4] have used ultrasound assisted casting technique, which uses high-intensity ultrasonic waves to break the particles clusters in the molten metal [8], to disperse the particles more uniformly. Ershadul *et al.* [3] and Chen *et al.* [9] have incorporated Al_2O_3 nanoparticles (1.5wt% and 3wt%, respectively) into different magnesium alloys using disintegrated melt deposition (DMD). This process combines conventional casting and spray casting. Avoiding the difficulty of wetting nanoparticles with the molten metal, powder metallurgy has also been used by Wong *et al.* [10].

In the present study, Friction Stir Processing (FSP), a solid-state processing technique derived from Friction Stir Welding (FSW), has been used in order to fabricate Mg based nanocomposites reinforced with Y_2O_3 particles. During the process, a non-consumable rotating tool penetrates in the material and advances along the processing area. The heat generated by friction of the tool turns the material malleable. The material flow follows the movement of the tool, from the front to the back of the tool and around the pin, where it cools down [11]. The large plastic deformation involved in the process leads to a solid-state mixing between the particles and the base material due to the fragmentation and redistribution of particles [12, 13].

FSP is an interesting technique for the processing of metal matrix composites, since it leads to a better

bonding between the reinforcement and the matrix, when compared to other processes involving casting [14, 15, 16]. FSP has already been employed for the elaboration of magnesium based nanocomposites. Lee *et al.* [17] have incorporated SiO_2 nanoparticles into an AZ61 magnesium alloy. The SiO_2 particles lead to an improvement of the hardness and the wear property in the stir zone. Faraji *et al.* [18] have incorporated 30 nm-sized Al_2O_3 particles. They have reported an improvement in the wear resistance for the composite and shown the importance of the processing parameters for obtaining a better particles distribution. Recently, Mertens *et al.* [19] have incorporated short carbon fibers in different magnesium alloys (AZ31B and AZ91D) using FSP. The presence of the reinforcement reduces the grain size and increases the yield strength from 15 to 25%.

Most of these studies show that the ability to disperse particles during the elaboration of nanocomposites plays a key role in the mechanical performance of the obtained nanocomposite and particles clustering has been associated with a loss of ductility [20]. However, very few studies provide a well documented 3-D characterization and quantification of the 3-D dispersion of particles in nanocomposites [21]. Given the ability of an heterogeneous distribution of reinforcements to limit the mechanical properties of nanocomposites, it is important to have a quantitative description of the spatial distribution of these particles as done in [22].

Strengthening mechanisms associated with particles-dislocations interactions have been traditionally treated with "averaged" microstructural properties, such as particles volume fraction and average particles size. However, there are now evidences which indicate that the overall strength of the material is affected by the particles size and spatial distribution [23].

The aim of the present paper is to investigate in depth the spatial and size distribution of Y_2O_3 particles in Mg-based nanocomposites processed by FSP and more precisely:

- how FSP processing parameters can be optimized to control particles spatial distribution,
- how particles size and spatial distributions impact the relevant strengthening mechanisms in nanocomposites.

In a fist part, FSP processing parameters are determined considering spatial distribution of particles measured on X-Ray micro-tomographic images in order to process an optimum nanocomposite. In a second part, an extended 3D multi-scale characterization analysis using different X-ray tomographic techniques is presented. It allows the detailed investigation of the spatial distribution of Y_2O_3 particles across four orders of magnitude of particles size. Finally, congruous micro-mechanical models using the real particles size and spatial distributions are either adapted either specially developed to account for particles distribution on strengthening mechanisms.

2. Materials and experimental procedures

2.1. Materials

Magnesium matrix nanocomposites were elaborated from 99.95% purity magnesium plates (from Magnesium Elektron) and Y_2O_3 powder. The detailed chemical composition of the magnesium plates provided by the supplier is given in Table 1. The original Y_2O_3 powder has a mean diameter of 3.5 μm [24]. The main advantage of using Y_2O_3 powder is its high thermal and chemical stability, which avoids the formation of matrix/particles reaction by-products as observed for instance in [25]. In addition, due to the large difference between the atomic number (Z) of Y_2O_3 (Z = 20.4) and Mg (Z = 12), Y_2O_3 generates a good contrast with respect to the magnesium matrix on 3-D tomographic images.

Table 1: Chemical composition of magnesium plates used in this study.

Element	**Quantity (wt. %)**
Mg	Balance
Al	<0.005
Cu	<0.005
Fe	<0.005
Mn	<0.02
Ni	<0.005
Si	<0.01

2.2. Friction stir processing

FSP is performed under displacement control on a HERMLE milling machine where a rotating tool is mounted. In the present case, the workpiece is an as-rolled magnesium plate with the following dimensions : 3 mm thickness, 250 mm length and 48 mm width. A linear groove (1 mm depth, 220 mm length and 2 mm width) is machined along the centerline of the plate. The linear groove is filled with Y_2O_3 powder (around 0.5 g) and is then covered with a 0.5 mm thick magnesium plate (with identical composition as the base material) in order to avoid powder loss during the process. The experiment set up is shown in Figure 1(*a*). The whole assembly is tightly fixed to a backing plate with two clamps. The clamps provide a rigid fixing, ensuring the tight fitting of the thin magnesium plate with the 3 mm thick plate. The 80 mm thick backing plate and the two clamps are both made of high carbon steel. The experiment is installed in a tank fulfilled with cutting oil in order to ensure the cooling of the backing plate. The FSP tool made of H13 steel has a 20 mm diameter scrolled shoulder and a 2 mm long M6 threaded Triflat pin (three sides of a hexagon inscribed in the circle of the pin, see [26] for a schematic of the tool geometry). The tool is tilted backwards by an angle of 1°.

The final microstructure and particles distribution are highly dependent on the process parameters, such as rotational speed, advancing speed and tool geometry [27]. Different processing parameters (see Table 2) are thus tested in order to obtain the most homogeneous particles dispersion. Each set of parameters is applied to one workpiece and a total of 6 workpieces have been processed. For the sake of comparison, pure magnesium samples were processed by FSP using two magnesium plates without powder and are called reference samples.

Three series of FSP passes are carried out successively on each workpiece. Each series comprises a first pass on the center axis (corresponding to the axis where the groove fulfilled with Y_2O_3 powder is located), a second pass shifted by 1.5 mm from the center axis on the advancing side and a third pass shifted by 1.5 mm from the center axis on the retreating side (Figure 1(a)). The advancing side (AS) corresponds to the side where the rotational tool movement is in the same direction as the advancing movement, while the retreating side (RS) is the opposite side. The tool displacement is parallel to the rolling direction of the magnesium sheets. A large number of passes (3x3) is chosen in order to reduce the clustering of reinforcements [28, 29, 17].

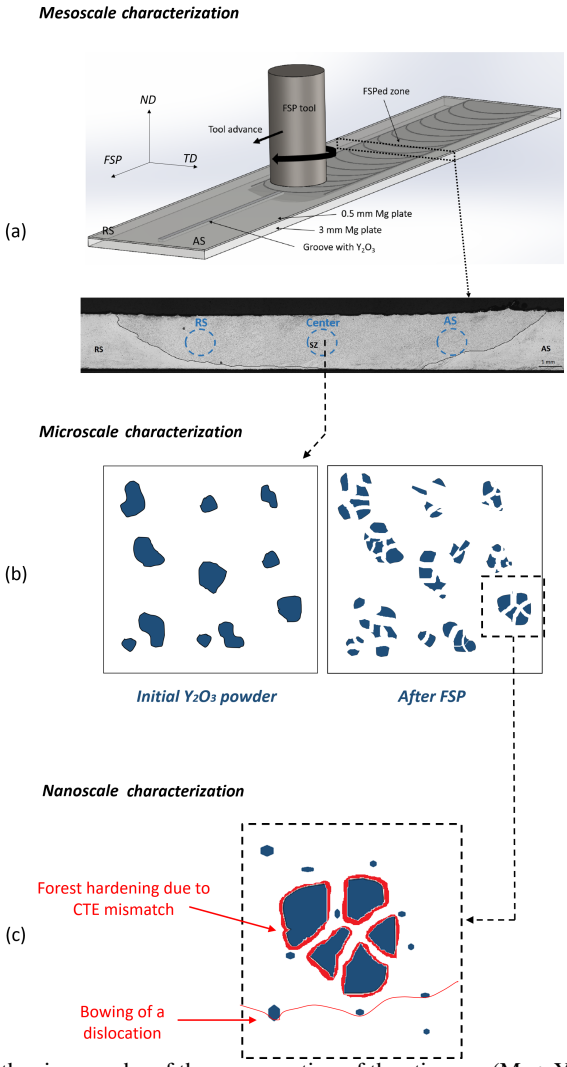

Figure 1: Schematic of FSP with micrography of the cross-section of the stir zone (Mg+ Y_2O_3 sample, FSP parameters: ω = 1500 rpm and v = 500 mm/min) in a plane perpendicular to the tool advance direction with visualization of the 3 specimens locations for laboratory tomography (AS = advancing side, RS =retreating side) (a). Schematic scenario of the microstructural evolution: FSP breaks the Y_2O_3 particles into smaller fragments (b). Zoom in (b): GND close to the large Y_2O_3 particles and dislocation bowing around smaller fragments (c).

2.3. Multiscale microstructural characterization methods

The original Y_2O_3 powder is fragmented during the elaboration of the nanocomposite by FSP. The size of Y_2O_3 particles found in the stir zone can be categorized in three groups according to their sizes. The first group consists of large Y_2O_3 particles with a typical size larger than 1 μm which corresponds to clusters of

Table 2: Process parameters used for the fabrication of the friction stir processed samples: advancing speed (v), rotational speed (ω) and amount of Y_2O_3 particles.

Materials	**v** (mm/min)	ω (rpm)	$\mathbf{Y_2O_3}$ (g)
Mg	300	1500	-
Mg	500	1500	-
Mg	500	1000	-
Mg+Y_2O_3	300	1500	0.526
Mg+Y_2O_3	500	1500	0.457
Mg+Y_2O_3	500	1000	0.461

powder particles which were left intact or broken into large fragments during processing. The second group of particles with an intermediate size of a few hundreds of nanometers corresponds to the fragmentation of the initial clusters of powder particles. Finally, a third group composed of the smallest particles with a size ranging from one hundred of nanometers down to a few nanometers results from the fragmentation of the individual polycristalline powder particles. A 3-D multiscale characterization is thus necessary to capture all the microstructural information across multiple length scales. As an increase of resolution usually comes at the expense of analysed volume, a multiscale characterization involving three different techniques will be used to study the microstructural heterogeneities at three relevant length scales, as detailed hereafter.

2.3.1. Mesoscale characterization

Material flow within the stir zone is complex and can result in heterogenous microstructures between the three different locations defined as the center of the stir zone, the retreating side (RS) and advancing side (AS) [12]. An optical image of the cross-sectioning of the weld along a plane perpendicular to the tool advance direction is presented in Figure 1(a) and shows the different zones of the weld. In order to identify the set of parameters ensuring the most homogeneous particles distribution within the stir zone, three cylindrical samples (800 μm diameter and 1.8 mm height) are extracted in the center, AS and RS zones of each FSPed nanocomposite samples (see Figure 1(a)) and characterised by laboratory tomography. Tomographic scans are performed on a Nanotom XL from RX Solution with a Quadro 4320 detector and a nanofocus X-ray tube. The resolution of the laboratory tomography (voxel size of 0.5 μm) allows us to characterize large particles and clusters of particles (up to a few μm) over a large volume ($\approx$ 0.1 mm^3).

Considering the achieved resolution, laboratory tomographic scans will hence give access to the breaking and redistribution of large particles all over the FSPed zone but not to intermediate and small particles. Y_2O_3 reinforcement particles were also characterized based on Scanning Electron Microscope (SEM) images.
In order to reveal the grain boundaries and FSP zone macrostructure, FSPed reference samples were etched using Nital solution (5 mL of nitric acid and 95 mL of ethanol) and FSPed samples with Y_2O_3 particles (Mg+Y_2O_3) with acetic picral (5 g picric acid, 10 mL acetic acid, 100 mL ethanol and 10 mL H_2O), see Figure 1(a).

2.3.2. Microscale characterization

Synchrotron X-ray nanoholotomography was used in order to quantitatively characterize the size and spatial distribution of particles with intermediate size, i.e. a size of a few hundreds of nanometers. Synchrotron X-ray nanoholotomography scans were performed on ID16A nano-imaging Beamline at the European Synchrotron Radiation Facility (ESRF). Radiographs were taken at four sample-source distances while keeping the detector position fixed. The distances were modified in order to obtain a voxel size of 25x25x25 nm^3 and a field of view of 50μmx50μmx25μm. Since the sample diameter (500 μm) is significantly larger than the field of view, local tomography is performed after selecting the relevant region of interest from a low resolution tomography scan previously recorded. Further details about the imaging set-up can be found in [30].

2.3.3. Nanoscale characterization

Transmission electron microscopy (TEM) was used to study the smallest particles (smaller than a hundred of nanometers). TEM foils were sampled at 1 mm beneath the top surface such that the TEM foil normal is along *ND* defined in Figure 1(a). These foils were first mechanically thinned down to 100 μm and then electrochemically polished using a solution of perchloric acid (1%) and ethanol at 50 V and -5°C. TEM micrographs with a resolution of approximately 2 nm were taken on a LaB6 Jeol 2010 with an accelerating voltage of 200 kV. *In situ* TEM experiments using thermal cycling, between room temperature and 400°C, were also performed on a LaB6 Jeol JEM-2010 microscope at 130 kV in order to investigate the dislocation-particle interactions in the nanocomposite.

2.4. Texture analysis

X-ray diffraction measurements were performed in the gage length of the sample that corresponds to the SZ, on both the base Magnesium plates and the FSPed plates, with and without particles. Incomplete pole figures were obtained as the tilt angle χ from the normal direction of the sample surface varies from 0° to 75°.

2.5. Mechanical characterization

Tensile tests were performed at room temperature on FSPed reference samples and nanocomposites in order to quantify the effect of the addition of Y_2O_3 particles on the yield stress and the strain hardening behavior of nanocomposites.

Two flat tensile specimens were extracted inside the stir zone of the FSPed samples (reference samples and nanocomposites) such that the tensile direction is along the process direction (FSP, defined in Figure 1(a)) and the gage zone within the SZ zone . The samples were fabricated using electrical discharge machining (EDM) with a gage width, length and thickness of, respectively, 1.5 mm, 3 mm and 1.5 mm. Tensile tests were performed using a Gatan Microtest MT2000EW tensile stage (*ex situ*) with a cross head velocity of 7.10^{-2}mm/min and an initial engineering strain rate of 4.10^{-4} s^{-1}.

3. Experimental results

Firstly, the results of the laboratory and SEM analysis are presented in order to select the best processing parameters for producing an ”optimum” nanocomposite with optimum dissociation of the clusters of initial powder particles. Then, the results of the X-ray tomography, TEM and mechanical characterizations of this optimum nanocomposite are presented.

3.1. Effect of FSP parameters on particles distribution at the mesocale

The effects of FSP processing parameters (see Table 2) on the grain size, proportion and distribution of Y_2O_3 particles in the Stir Zone (SZ) are detailed hereafter.

Grain size

Figure 2 shows a macrograph of the transverse cross-section of one typical FSPed sample, the Mg+Y_2O_3

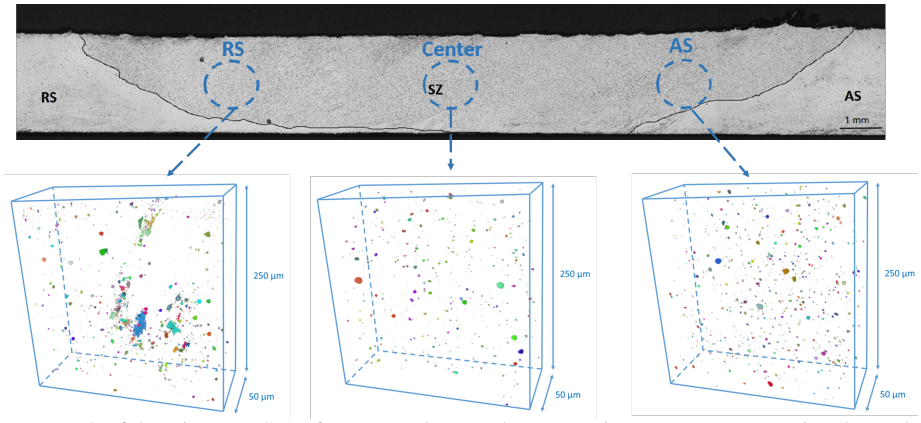

Figure 2: Macrograph of the stir zone (SZ) of a Mg+Y_2O_3 sample (processing parameters: rotational speed of 1500 rpm and advancing speed of 500 mm/min) schematically representing the locations of the laboratory tomographic scans (RS = retreating side and AS = advancing side) and their corresponding 3-D images of Y_2O_3 particles . Each distinct particle is shown in a different color.

sample processed using a rotational speed of 1500 rpm and advancing speed of 500 mm/min. The stir zone (SZ) presents a basin shape morphology and is almost symmetric in both advancing AS and RS. Thermo-mechanically affected zone or heat affected zones are difficult to identify. During FSP, a dynamic recrystallization takes place and the grain size is reduced [31, 32]. Indeed, the average grain size of the as-received magnesium plates is about 50 μm and is reduced to a mean grain size close to 10 μm after FSP regardless of the processing parameters or the presence of Y_2O_3 particles (see supplementary material for more details). This is probably due to the low amount of Y_2O_3 particles that has been added (see Table 2). A higher volume fraction of particles would have lead to smaller grains in the nanocomposites than in pure Mg FSP samples since the Y_2O_3 particles can restrain grain growth after recrystallization, during the cooling stage [33, 34].

Volume fraction of Y_2O_3 particles

Table 3 shows the surface (f_s) and volume (f_v) fractions of Y_2O_3 particles measured based on SEM micrographs and on laboratory tomography scans (three scans per sample), respectively. SEM micrographs used for the surface fraction have been taken in different regions of the stir zone. Furthermore, the volume fraction is averaged over the three tomography samples (center of the stir zone, RS and AS, see section 2.3.1). The surface and volume fraction given in Table 3 are thus representative of the particle content within the whole stir zone.

SEM micrographs were taken at a magnification between 1400x to 4300x allowing a statistical analysis

Table 3: Characterization of the Y_2O_3 particles in the Mg + Y_2O_3 samples. Surface fraction (f_s) was obtained from SEM micrographs, while volume fraction (f_v) and mean equivalent particle diameter ($D_{eq-mean}$) from laboratory tomography scans. The equivalent diameter of a particle is the diameter of a sphere with the same volume.

Processing parameters	$\mathbf{f}_s$ **(%)**	$\mathbf{f}_v$ **(%)**	$\mathbf{D}_{eq-mean}$ **(μm)**
v=300mm/min, ω=1500rpm	0.54±0.12	0.037±0.015	2.1±0.14
v=500mm/min, ω=1500rpm	0.26±0.09	0.021±0.006	2.2±0.05
v=500mm/min, ω=1000rpm	0.73±0.16	0.025±0.009	2.1±0.13

of particles larger than approximately 100 nm. It means that the first group of large Y_2O_3 particles (size larger than 1 μm) and the intermediate family of particles (few hundreds of nanometers) are taken into account for the surface fraction. On the opposite, the resolution of the laboratory tomography only allows us to observe particles larger than approximately 1 μm, i.e. only the first group composed of the largest particles. This explains why the surface fraction of particles is much larger than the volume fraction (Table 3).

Table 3 indicates that for a fixed rotational speed, a lower advancing speed leads to a higher surface fraction of Y_2O_3 particles. Furthermore, for the same advancing speed, a lower rotational speed leads to a higher surface fraction of Y_2O_3 particles. It has been defended in the litterature [19, 35] that an increase of the heat input, i.e. a lower advancing or higher rotational speed, leads to a wider dispersion of the stir zone. This should result in a lower volume fraction of reinforcements. As in our case the surface of the stir zone is found similar for all processing conditions, this effect is very limited and variation of f_s could be attributed to particles loss during the process. It has also been reported that a higher advancing speed [19] or a higher rotational speed [36] induces the fragmentation of the reinforcement into smaller fragments. The sample processed with an advancing speed of 500 mm/min and a rotating speed of 1500 rpm is hence expected to fragment the Y_2O_3 particles into smaller fragments. These very small fragments are hardly identified by SEM and this sample has the lowest surface fraction of Y_2O_3 (f_s = 0.26%).

The mean particles diameter determined from the laboratory tomography (Table 3) is close to 2.1 μm for all conditions. As already explained, only the larger particles which have not been well fragmented are detected

by this technique. The size of these large fragments is thus more dependant on the initial powder size (3.5 μm) than the FSP parameters.

Spatial distribution of Y_2O_3 particles

Figure 2 shows the 3-D tomography perspectives of particles distribution in AS, Center and RS of the sample processed with a rotational speed of 1500 rpm and advancing speed of 500 mm/min). Each particle is shown in a different color in order to highlight that clusters of particles are actually composed of large particles surrounded by many smaller ones. A quantitative analysis of the particles distribution was then performed on each the 3 FSPed nanocomposite samples in order to select the processing parameters leading to the most homogeneous particles distribution.

If a point represents the center of each particle, a simple characterization of the particles spatial distribution can be established by comparing the mean and the variance of the measured nearest-neighbours distances with the values calculated for an ideal random arrangement (a Poisson distribution [37, 38, 39]). The parameter Q is defined as the ratio of the experimental mean nearest-neighbor distances to the mean nearest-neighbor distance of a Poisson distribution. Similarly, the parameter R is defined as the ratio of the experimental variance of nearest-neighbor distances to the variance of the nearest-neighbor distances of a Poisson distribution. The combination of Q and R allows us to distinguish between random sets ($Q \approx 1$, $R \approx 1$), short-range ordered sets ($Q > 1$, $R < 1$), clustered sets ($Q < 1$, $R < 1$), and sets of clusters with a superimposed background of random points ($Q < 1$, $R > 1$) [37]. The expressions for the expected mean and variance for a 3-D Poisson distribution are given in [38] :

$$mean(D_{c-c}^{Poisson}) = 0.893(\frac{4}{3}\pi\rho)^{-1/3} \tag{1}$$

$$var(D_{c-c}^{Poisson}) = 0.105(\frac{4}{3}\pi\rho)^{-2/3} \tag{2}$$

where D_{c-c} is the center-to-center distance and ρ is the volume density of particles.

Figure 3(a) presents the Q and R ratios for the three different regions of the stir zone (RS, Center and AS) for the three sets of FSP parameters. Whatever the processing parameters used, all the tomographic samples extracted in the center and in the AS have a quite random distribution of particles, indicating a limited tendency to clustering (i.e. $Q \approx 1, R \approx 1$). In the retreating side of the stir zone, the analysis indicates

the presence of clusters superimposed on the random distribution (i.e. $Q < 1$, $R > 1$) for two sets of FSP parameters (v=300 mm/min, ω=1500rpm and v=500 mm/min,ω=1000rpm, respectively samples 1 and 3 in Figure 3). The sample processed with the fastest advancing speed (v=500mm/min) and the fastest rotational speed (ω=1500rpm), i.e. sample 2 in Figure 3, has a quite random distribution of Y_2O_3 particles, even on the retreating side. Figure 3(*b*) shows 3-D perspectives of particles distribution in the RS for each set of FSP parameters. It is quite clear that clusters of particles are found in sample 1 and 3 while it seems more homogeneous for sample 2.

Optimum processing parameters

A more homogeneous dispersion of Y_2O_3 particles is observed when using a higher rotational speed (1500 rpm) and a higher advancing speed (500 mm/min). The nanocomposite processed using this set of parameters will be called optimum nanocomposite in the following. The next section will be dedicated to the detailed microstructural and mechanical characterization of the optimum nancomposite.

3.2. Multiscale characterization of the particles

A 3-D multiscale characterization of the Y_2O_3 particles in the SZ at a higher resolution than the one achieved with laboratory tomography is performed on the optimum nanocomposite using 3-D nanoholotomography and TEM in order to quantify particles size and spatial distribution.

Size distribution

Figures 4(*a*), (*b*) and (*c*) show the number-weighted and volume-weighted cumulative size distribution of the particles observed by laboratory tomography, nanoholotomography and TEM, respectively. The equivalent diameter D_{eq} of a particle corresponds to the diameter of a sphere of same volume. It is clear that the used multi-scale procedure coupling laboratory tomography, nanoholotomography and TEM allows us to characterize particles across four orders of magnitude (i.e. particle size ranging between a few *nm* up to 10 μm).

Figure 4(*b*) shows that approximately 90% of the Y_2O_3 particles (number-weighted) are smaller than 500 nm. These small particles, however, only contribute to about 30% of the volume fraction of particles. The global volume fraction of particle F_v^{Global} is equal to 0.33%, in reasonable agreement with the surface fraction of particles measured by SEM (0.26% for the selected nanocomposite, see Table 3).

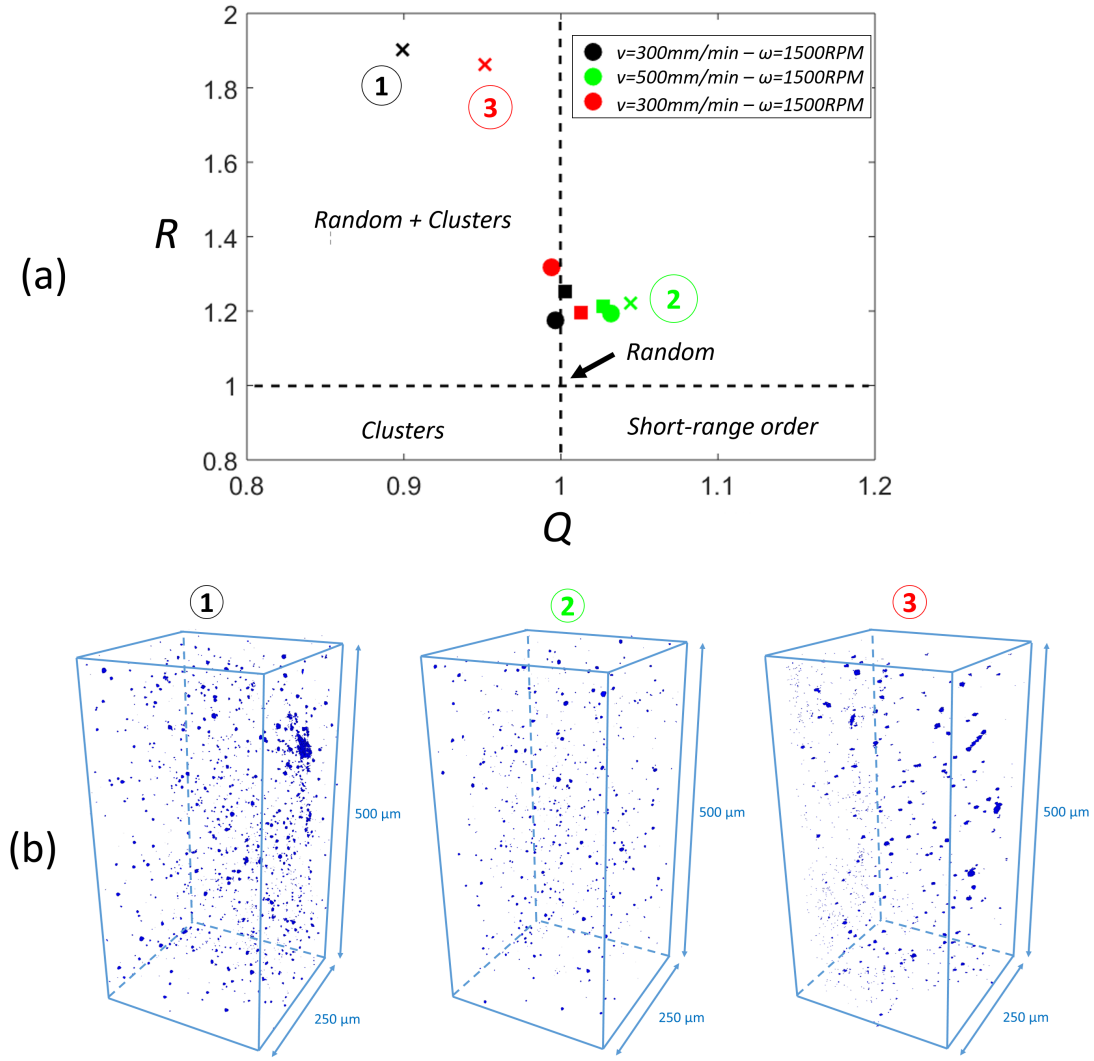

Figure 3: (*a*) Characterization of Y_2O_3 particles spatial distribution based on the normalized mean and variance of the nearest-neighbor distance in the different regions of the stir zone for the three sets of FSP parameters. Circle, square and cross dots indicate samples extracted in the retreating side, center and advancing side of the stir zone, respectively. (*b*) 3-D laboratory tomography perspective of Y_2O_3 particles distribution for the specimen extracted in the retreating side of the sample for the three sets of FSP parameters.

It was also shown in Section 3.1 that the volume fraction of particles observed by laboratory tomography is quite low (0.021% for the optimum nanocomposite, see Table 3). This can be explained based on Figure 4(b): particles larger than 1 μm represent a small fraction (approximately 20%) of the total volume

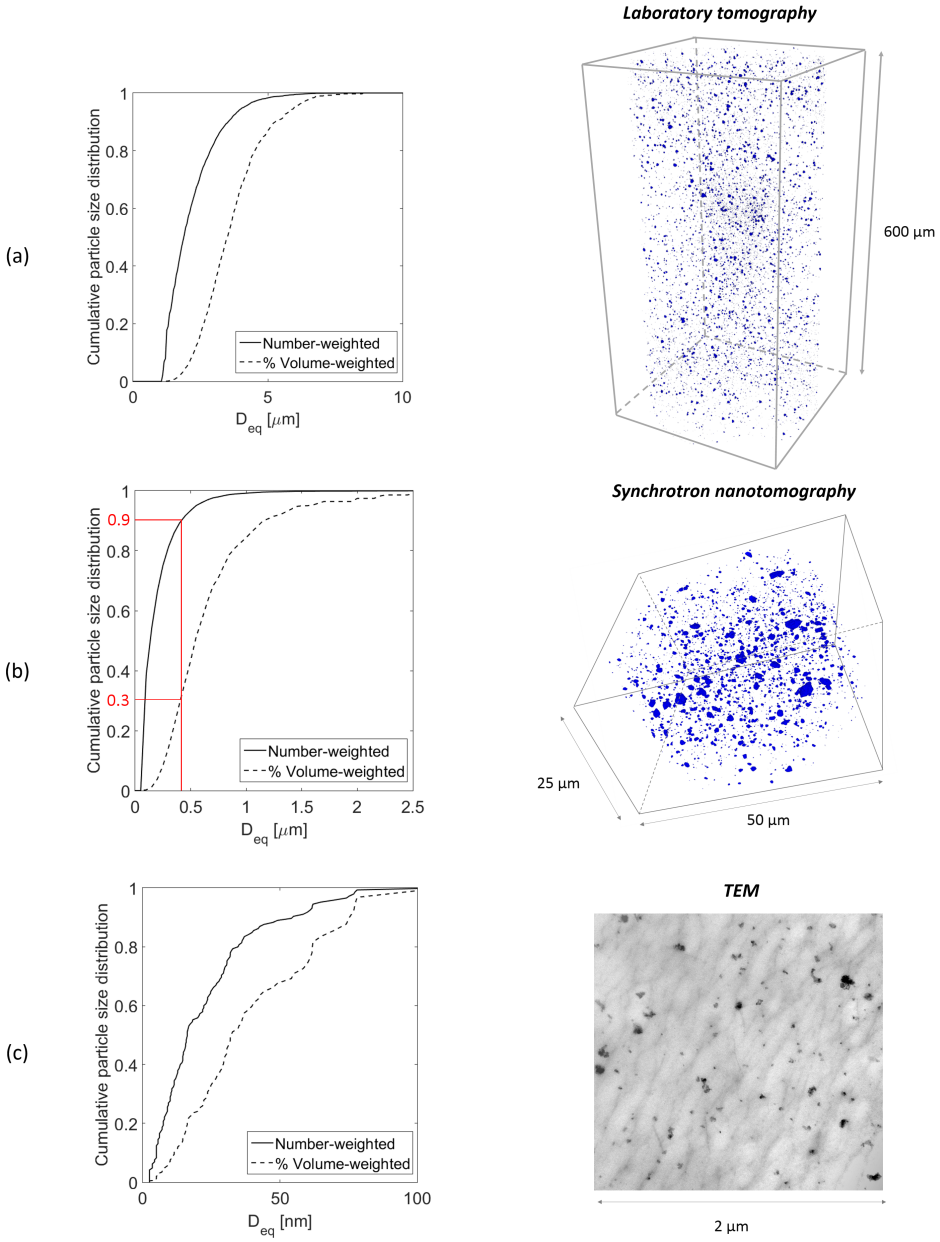

Figure 4: Number-weighted and volume-weighted cumulative size distributions of Y_2O_3 particles of the optimum nanocomposite measured on a 3-D laboratory tomography rendering (*a*), nanoholotomography rendering (*b*) and TEM bright field micrographs (*c*). The equivalent diameter D_{eq} of a particle corresponds to the diameter of a sphere of same volume.

of particles. Since only these particles are imaged with laboratory tomography, it justifies that the F_v^{Global} measured with laboratory tomography is one order of magnitude smaller than the F_v^{Global} measured with nanoholotomography.

Short-range neighboring

A 3-D finite body tesselation has been applied in order to characterize the short range neighboring of these particles. In this method, a network of cells is constructed around each particle in such a way that every point within a cell is closer to the corresponding particle than to any other [40, 41]. It is thus very similar to a simpler Voronoi tessellation, except that in this case the tesselation is based on the whole particles and not only on the centroids of the particles (see Figure 5(a) for a schematic of the procedure in 2-D). A 3-D visualization of this procedure applied for the synchrotron X-ray nanoholotomography images is shown in Figure 5(b), where Y_2O_3 particles and tessellated cells are in blue and grey respectively. Tessellated cells are generally used to compute local indicators on a particle-by-particle basis of the homogeneity a particles distribution as for instance in [42]. Among these local indicators, the local volume fraction of particle (F_v^{Local}) is defined as the ratio of the particle volume to the volume of its associated cell.

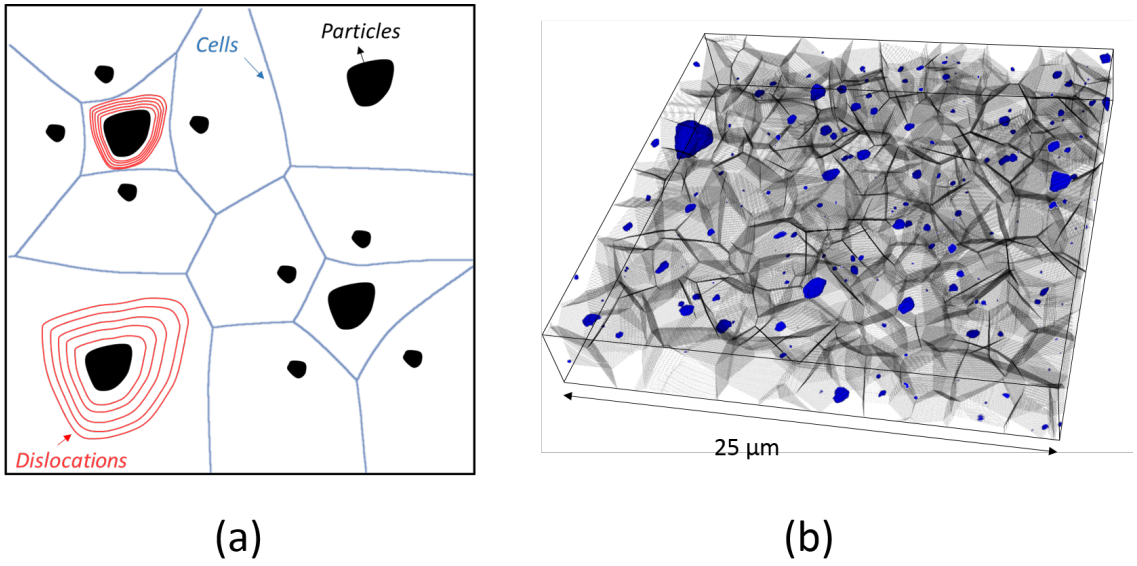

Figure 5: Example in 2-D of the watershed cells of the particles (*a*). For two identical particles, the GND density is higher for a particle embedded in a smaller cell (i.e. in a dense region) compare to an isolated particle. Visualization of the result of the finite body tesselation procedure applied in 3-D to a sub-box of the nanoholotomography image (*b*). Y_2O_3 particles are in blue and cells are in grey.

The parameter F_v^{Local} is normalized by the global volume fraction of particle ($F_v^{Global} = 0.33\%$) in such a way that a ratio $\frac{F_v^{Local}}{F_v^{Global}}$ smaller or larger than one indicates isolated particles or particles with neighbours in close proximity, respectively. Figure 6 shows the distribution of $\frac{F_v^{Local}}{F_v^{Global}}$ associated with each particle. As it can be clearly seen in Figure 6, the ratio $\frac{F_v^{Local}}{F_v^{Global}}$ increases with the equivalent diameter D_{eq} i.e. the larger the particle, the higher the chances that it is located in a volume densely filled with particles. This can be explained by the progressive breaking of the particles with the number of FSP passes. Large μm-sized Y_2O_3 particles are broken into smaller fragments dispersed at the subsequent FSP passes. The particle size progressively decreases with the number of passes. However, a few large particles are broken into smaller fragments during the last passes and these fragments remain in close proximity to the parent particle. A more detailed discussion of this phenomenon can be found in [41].

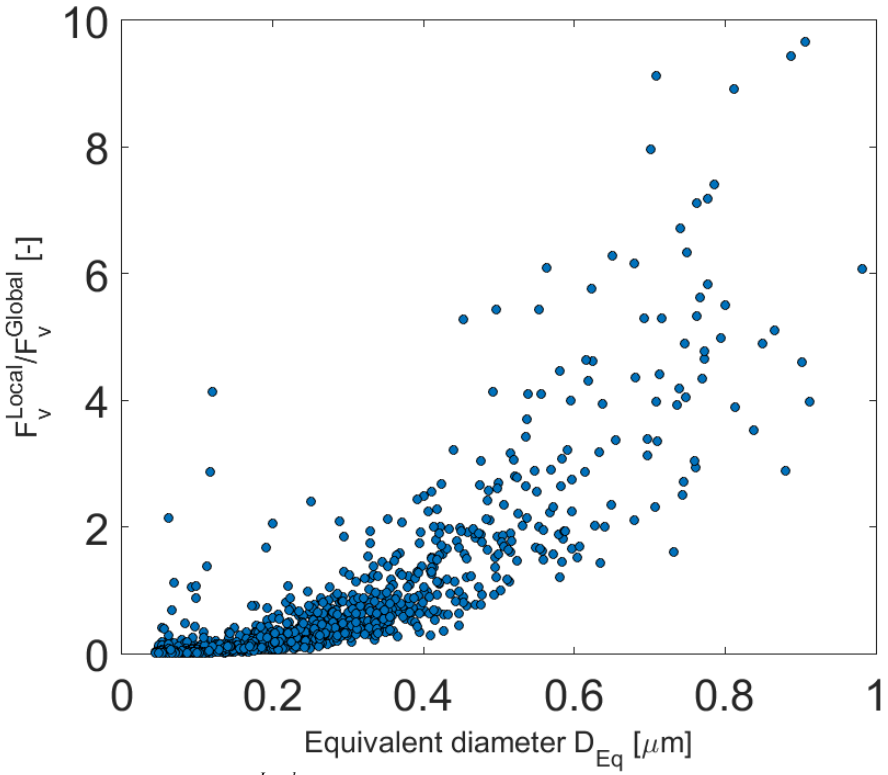

Figure 6: Local volume fraction F_v^{Local} resulting from the finite body tessellation normalized by the global volume fraction F_v^{Global} as a function of the particle size.

Table 4: Mechanical properties of pure magnesium and nanocomposite: yield strength (YS), ultimate tensile strength (UTS), ductility (fracture strain) and strain hardening rate (Θ_0).

Properties	**Mg**	**Mg+Y_2O_3(0.33%)**
0.2 % YS (MPa)	52.4±2.5	68.7±1.8
UTS (MPa)	115.2±1.1	142.1±8.6
Ductility (%)	26.4±3.6	22.5±2.6
Θ_0 (MPa)	635±112	1062±31

3.3. Mechanical properties

In this section, the tensile mechanical behavior of the optimum nanocomposite is studied as well as texture and TEM analysis of particles / dislocations interactions.

Figure 7(a) shows the true stress strain response of tensile samples extracted from the optimum nanocomposites and from the reference sample (pure magnesium processed with the same FSP parameters : v = 500 mm/min and ω = 1500 rpm). Their corresponding mechanical properties are presented in Table 4.

An improvement of the yield strength (YS) and the ultimate tensile strength (UTS) is observed for the nanocomposite and will be analysed in details in section 4. The addition of particles does not have a strong impact on the ductility : the observed decrease of fracture strain with the addition of Y_2O_3 particles is not significant considering the inherent statistical variability in damage mechanisms. This could be due to

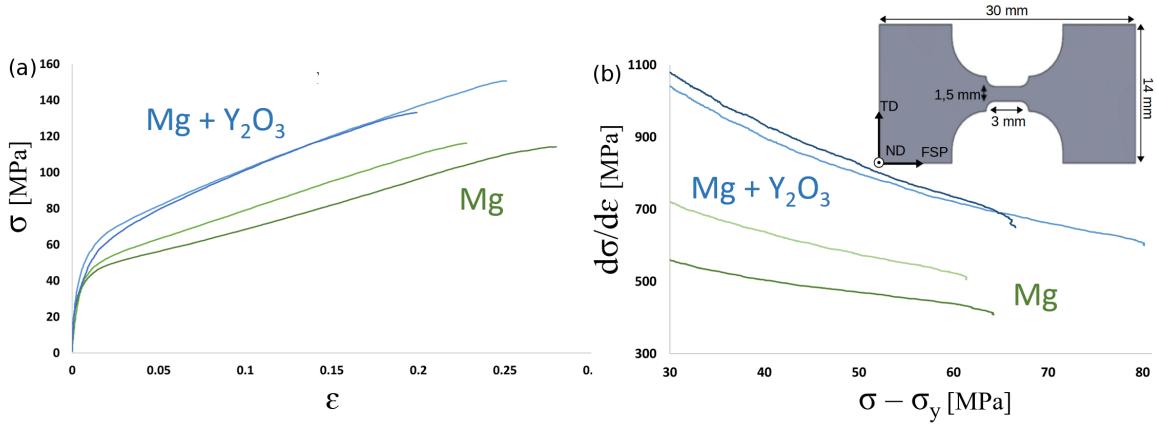

Figure 7: True stress vs. true strain tensile loading curves for pure magnesium and nanocomposite with initial engineering strain rate of 4.10^{-4} s^{-1}. Each curve corresponds to a tested specimen (a). Kocks plot for pure magnesium and the nanocomposite (b). Inset gives the specimen geometry and dimensions. Sample thickness is 1.2 *mm*.

the optimization of processing parameters in order to ensure a good breaking of clusters of particles (see Section 3.1), generally associated with a loss of ductility [20, 43]. A higher strain hardening coefficient is also noticeable in the samples containing Y_2O_3 particles, which is in agreement with [44, 45]. The increase in strain hardening is better evidenced in the Kocks plot given in Figure 7(b), where the hardening rate ($\Theta = d\sigma/d\varepsilon$) is plotted as a function of the stress level. The increase of the ultimate tensile strength is directly related to the higher strain hardening observed in the nanocomposite, which is confirmed by the increase of the initial hardening rate Θ_0 that describes the dislocation storage rate.

3.4. Microstructure

Texture analysis

A texture analysis has been performed in order to study the influence of FSP and of the addition of particles on the texture of magnesium. The as-received magnesium plates have a strong fibre texture in the (0002) pole figure: the basal planes are parallel to the rolling direction. This is the typical texture expected for magnesium plates [46]. The incomplete pole figures presented in Figure 8 show a reorientation of the *c*-axis between 20 to 30° towards the FSP direction in FSPed samples compared to the base material. Previous studies show a texture evolution within the process zone: the tilt of the *c*-axis with respect to the normal direction varies between 20 to 90° which is coherent with the observed texture ([47], [46]). No significant modification of the texture is observed after FSP with the addition of Y_2O_3 particles.

Considering the very strong texture observed on FSP samples, the Taylor factor M is assumed to be equal to the inverse of the Schmid factor (m) calculated for a single crystal with a misalignement angle between the *c*-axis and the loading axis between 60 and 70° based on Figure 8 :

$$m = cos(\alpha).cos(90 - \alpha) = sin(2\alpha)/2 \tag{3}$$

The Taylor factor value varies hence between 2.31 and 3.11.

Particles dislocations interactions

Two types of dislocation-particle interactions have been investigated by *in situ* TEM experiments using thermal cycling. Figure 9(a-d) shows a dislocation bowing around a Y_2O_3 particle, signature of Orowan

strengthening. It is clear from this example that particles, as small as a few tenth of nanometers, can already induce dislocation bowing. This observation suggests that Orowan strengthening is active for the smallest particles. Furthermore, these particles smaller than 50 nm represent 80% of the total number of particles observed in TEM foils (see Figure 4(c)). This means that the TEM is the relevant technique to characterize this strengthening mechanism.

The second type of dislocation-particles interactions is due to the difference between the coefficient of thermal expansion (CTE) of the magnesium matrix and the Y_2O_3 reinforcement particles. This CTE mismatch effect leads to the generation of geometrically necessary dislocations (GND) at the interface between the reinforcement and the matrix during cooling after FSP. A higher concentration of dislocations at the interface between the magnesium matrix and the Y_2O_3 particles have been observed on TEM images which would be consistent with the GND generation mechanisms. (Figure 9(e)).

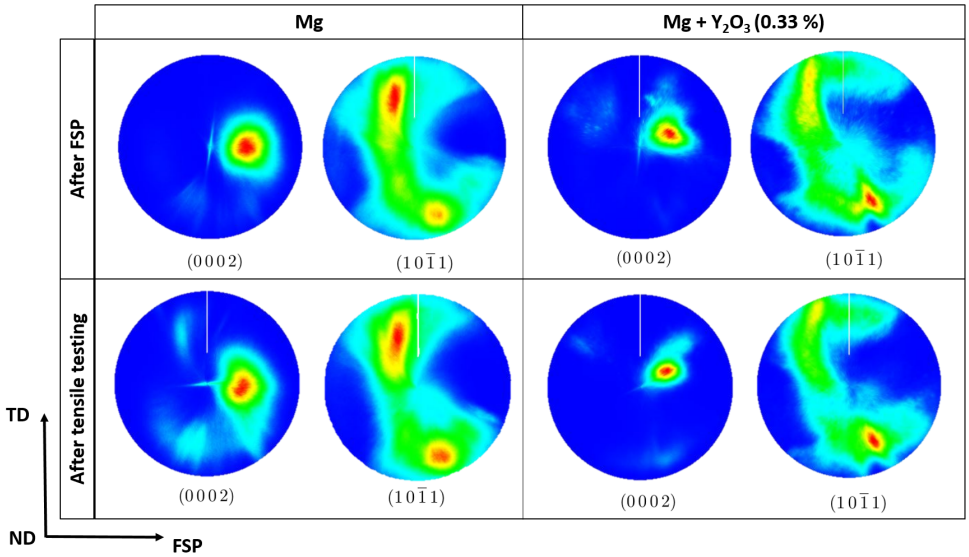

Figure 8: (0 0 0 2) and (1 0 $\bar{1}$ 1) incomplete pole figures ($0° < \chi < 75°$) obtained by X-ray diffraction of pure magnesium and optimum nanocomposite prior and after tensile testing. FSP direction is the same as the rolling direction of the original plates. Tensile direction is parallel to FSP direction.

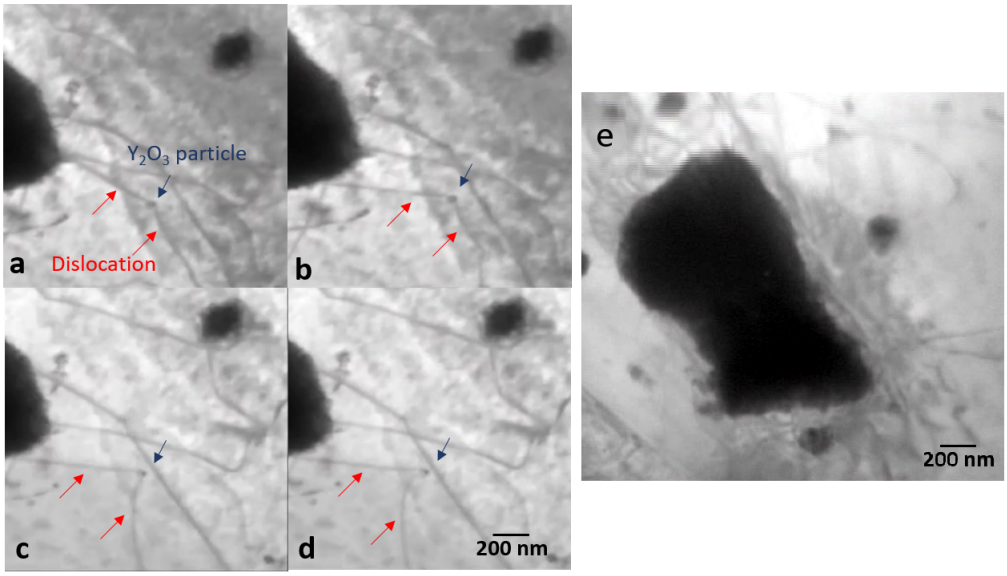

Figure 9: Bright field TEM (LaB_6 Jeol JEM-2010 MET at 130 kV) micrographs showing (a-d): dislocation bowing around a Y_2O_3 particle and (e): dislocations at the Y_2O_3 particle/matrix interface. Dislocations on the left part of the particle are not in diffraction condition due to a slight bending of the TEM foil around the particle.

4. Discussion

4.1. Identification of strengthening mechanisms

The improvement of the yield stress of the metal matrix nanocomposite with respect to the unreinforced magnesium could result from the contribution of different strengthening mechanisms: Hall-Petch strengthening, load transfer effect, Orowan strengthening and coefficient of thermal expansion (CTE) mismatch [48, 49, 50]. In addition, the mechanical behavior of magnesium is known to be strongly related to texture due to the HCP crystal structure of magnesium, which leads to a significant plastic anisotropy. The stress-strain response when tensile twinning is activated (tensile stress along the *c*-axis) can be completely different from the one obtained if tensile twinning is favorably oriented [51]. As detailed in Section 3.4, as the FSPed pure magnesium and the nanocomposite have very similar texture, the improvement of the yield stress cannot be attributed to a texture effect. Since magnesium deforms mainly by basal slip or twinning, the texture analysis indicates that the deformation occurs probably by basal slip. Twinning would promote a reorientation of the crystal and a misorientation would be observed on the pole figures after tensile testing, which is not the case (see Figure 8). A study of the deformation mechanisms when the same nanocomposite

is favorably oriented for twinning is presented in [52].

As mentionned in Section 3.1, the addition of Y_2O_3 particles has a very limited influence on the grain size : Hall-Petch strengthening cannot be the mechanism responsible for the strengthening observed in Figure 7(a). The load transfer effect takes into account the transfer of the load from the soft matrix (magnesium in the present case) to the hard reinforcement (Y_2O_3 particles) when an external load is applied. This contribution is proportional to the size and volume fraction of reinforcement. Since in the present case, the volume fraction of Y_2O_3 particles is low (only 0.33%, see Section 3.2), the contribution of the load transfer effect to the strengthening is expected to be negligible.

The small Y_2O_3 particles act rather as obstacles for dislocation movement (observed in Figure 9(a-d)) so that Orowan strengthening is expected to contribute to the macroscopic strengthening.

It can be concluded that the two mechanisms responsible for hardening are Orowan strengthening and CTE mismatch. In order to quantify the influence of particles distribution on these two mechanisms, parameters related to particles size and spatial distribution are introduced in analytical equations used to describe Orowan and CTE mismatch strengthening. The modified Orowan and CTE mismatch strengthening equations are presented in the next section.

4.2. Influence of particles size and spatial distribution on strengthening

Orowan strengthening is sensitive to the spatial distribution of particles [23]. In areas of the glide plane where the particle density is high, the particle spacing is reduced and the resistance to dislocation motion increases locally. On the opposite, a reduction in glide resistance is associated with the less populated areas appearing as the degree of clustering increases.

As observed in Figure 9(a-d), dislocation bowing is expected to occur for particles smaller than 50 nm. Nanoholotomography, with 25 *nm* resolution, does not allow us to capture accurately the size and the spatial distribution of the particles involved in Orowan strengthening which are hence characterized on TEM micrographs (see Section2.3.3) with a pixel size of approximately 2 nm, see Figure 10(a). Y_2O_3 particles observed in the micrograph are segmented by manual thresholding. Particles labelling (see Figure 10(b)) and parameters measurement are performed using MatLab [53].

Foreman and Makin [54] proposed an empirical expression to calculate the stress required to move a

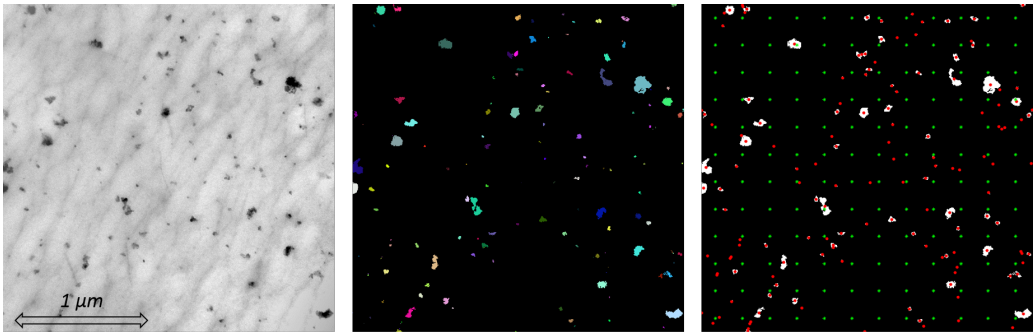

Figure 10: (*a*) TEM micrograph of the Y_2O_3 particles in the center of the stir zone of the nanocomposite. (*b*) Thresholding and labelling of the particles. (*c*) Visualization of the nodes grid and particles centroid to calculate the "aggregation parameter" P.

dislocation through an array of impenetrable obstacles randomly distributed (τ_c^{random}). De Vaucorbeil *et al.* [23] have used a modified areal-glide model to show that the effect of particles aggregation can be taken into account simply by dividing this empirical expression for τ_c^{random} by a so-called "aggregation parameter" P calculated from the spatial distribution of particles on the glide plane. In order to determine P, a regular grid of nodes is superimposed such that the node density is equal to the particle density, see Figure 10(c). The parameter P is then calculated as [23]:

$$P = \frac{1}{1.2L_s^2}\frac{1}{N_{nodes}}\sum_{i=1}^{N_{nodes}}\sum_{j=1}^{M_i}\frac{d_{ij}^2}{M_i} \tag{4}$$

where d_{ij} is the distance between the ith node and the centroid of its jth neighbouring particle, L_s is the average distance between particles ($L_s = \frac{1}{\rho_s}$, with ρ_s the number of particles per unit area) and M_i is the number of neighbouring particles for the ith node. A particle is considered as a neighbour of one node if no other particle lies in the smallest circle connecting these two. The parameter P is equal to 1 for a perfectly random distribution of particles and increases as the degree of clustering increases. For the experimental distribution of particles (Figure 10), the parameter P is equal to 1.22. This means that the distribution of small Y_2O_3 particles in Figure 10(a) is not far from a random distribution.

The modified empirical expression for the stress required to move a dislocation through the gliding plane

is then given by [23]:

$$\tau_c^* = \frac{\tau_{c,random}^*}{\sqrt{P}} = \frac{0.9\beta^{3/2}(1-\frac{\beta^5}{6})}{\sqrt{P}} \tag{5}$$

where β is the strength parameter of the obstacle to the dislocation motion ($\beta = \cos(\frac{\phi}{2})$ with ϕ the critical bowing angle) and $\tau_{c,random}$ is the critical shear stress for randomly distributed impenetrable obstacles. In this equation, τ_c^* is dimensionless and needs to be multiplied by $\frac{G_m b}{L_s}$ to obtain the corresponding absolute value, where G_m is the matrix shear modulus (16.5 GPa for pure magnesium [55]) and b is the Burgers vector magnitude (0.32 nm for magnesium).

Assuming that Y_2O_3 particles are impenetrable (i.e. $\beta = 1$), the Orowan contribution to strengthening is equal to 19.4 MPa. The contribution predicted by this simple model seems too large when compared with the experimental improvement(16.3 ± 2.1 MPa). Actually, this areal-glide model assumes that the line tension is constant and overlooks the self-interaction of a dislocation with its own stress field. As proposed by Bacon *et al.* [56], this interaction effect could be simply taken into account by saying that impenetrable obstacles can, when interactions are included, be treated as penetrable obstacles in the line tension model. Thus, if β is decreased from 1 to 0.7, the Orowan contribution to the strengthening is decreased to 13 MPa.

As for Orowan mechanism, the influence of particles size distribution on CTE mistach hardening is investigated. When the nanocomposite is cooled from the processing to room temperature, misfit strains are caused by the difference between the thermal expansion coefficients of the particle and the matrix and the associated thermal stresses can be sufficient to punch prismatic dislocation loops. GND are hence generated at the Y_2O_3 particle interface. The misfit strain due to the difference ΔCTE between the thermal coefficient of the matrix and the particle is given by [57]:

$$\epsilon_m = \Delta CTE.\Delta T \tag{6}$$

where ΔCTE is the difference between the coefficient of thermal expansion of the matrix and the reinforcement and ΔT is the difference between the temperature reached during FSP and room temperature. The coefficient of thermal expansion of magnesium and Y_2O_3 are, respectively, 25 and 8.1 10^{-6} K^{-1}. In the present study, the temperature in the SZ was not measured. As it depends on process parameters and especially on the ratio $\frac{\omega^2}{v}$, it can be approximated using the relationship validated by Commin *et al.* on AZ31

processed by FSP [58]. The obtained value of ΔT is 392K ± 40K. The number of dislocation loops generated in each direction on each particle in order to accommodate the misfit strain may be approximated by n_{GND}=D_{eq}.ΔCTE.$\Delta T/b$ [59]. It is not expected that particles smaller than a critical size contribute to strengthening if no prismatic loop is punched [20]. This critical diameter D_{eq}^{crit} is defined as the diameter for which a particle punches a single loop for each of the active glide direction and is given by D_{eq}^{crit}=$\frac{b}{\Delta CTE\Delta T}$, which gives a critical size of about 50nm. It is also in good agreement with the experimental observations showing that this phenomena occurs on large particles (a few hundreds of nm), see Section 3.4. Nanotomography is well suited to study this mechanism and a statistical analysis of particles larger than about 50 nm can be carried out.

The dislocation density ρ_{CTE} in the matrix due to punching can be calculated by [57]:

$$\rho_{CTE} = \frac{B f_p \epsilon_m}{b(1 - f_p)} \frac{1}{t} \tag{7}$$

where B is a geometric constant (12 for equiaxed particles), t is the smallest dimension of the particle (D_{eq} for a spheroidal particle) and f_p is the volume fraction of particles.

The contribution of this dislocation density to the strengthening of the composite can be calculated by the classical Taylor relationship [57]:

$$\Delta\sigma_{CTE}^{Global} = MAG_m b \sqrt{\rho_{CTE}} \tag{8}$$

where M is the Taylor factor (≈ 2.5, see Section 3.4), A is the strain-hardening constant with a value taken equal to 0.5 (between 0.3 and 0.6 for metals [60]). If the dislocation density is uniform in the matrix as it is often assumed, then the contribution to the strengthening $\Delta\sigma_{CTE}^{Global}$ is equal to 15.1 ± 1.5 MPa. The term "global" refers to the fact that in this case, the global volume fraction of particle F_v^{Global} = 0.33% and the average equivalent diameter of particles D_{eq} = 217 nm measured by nanotomography have been used.

However, the local dislocation density is not uniform: different sizes of particles generate a different number of GND. Furthermore, for a similar size of particle (and thus a similar number of punched dislocations n_{GND}), the density of dislocations is higher in the vicinity of particles in particle-rich regions [20],

as illustrated in Figure 5(a). In order to take this effect into account, the global volume fraction F_v^{Global} and the average equivalent diameter of particles D_{eq} are replaced by the local value associated with each particle. The distribution of the individual contribution of each particle to the strengthening $\Delta\sigma_{Local}$ is shown in Figure 11. In this case, the tessellation cells can be seen as a mesh of elements with each element associated to a certain stress. The macroscopic contribution from the distribution of $\Delta\sigma_{Local}$ is then given by the calculated cell-volume-weighted average $<\Delta\sigma_{Local}>$. The value of $<\Delta\sigma_{Local}>$ is found equal to 7.2 ± 0.7 MPa, indicating that the effect of the particles size and distribution inhomogeneity reduce by a factor 2 the strengthening contribution of CTE mismatch mechanism. From this analysis, it can be concluded that the inhomogeneity of the particles size and spatial distribution is expected to decrease more significantly the strengthening contribution from CTE mismatch compare to the Orowan contribution. Indeed, it has been shown that these two mechanisms are associated with two different sizes of particles : the analysis revealed that the spatial distribution of very small particles associated with the Orowan strengthening is almost random (P equal 1.22) and thus has only limited effect. On the opposite, the contribution from CTE mismatch is decreased by a factor 2 when taking into account the real spatial and size distribution of particles.

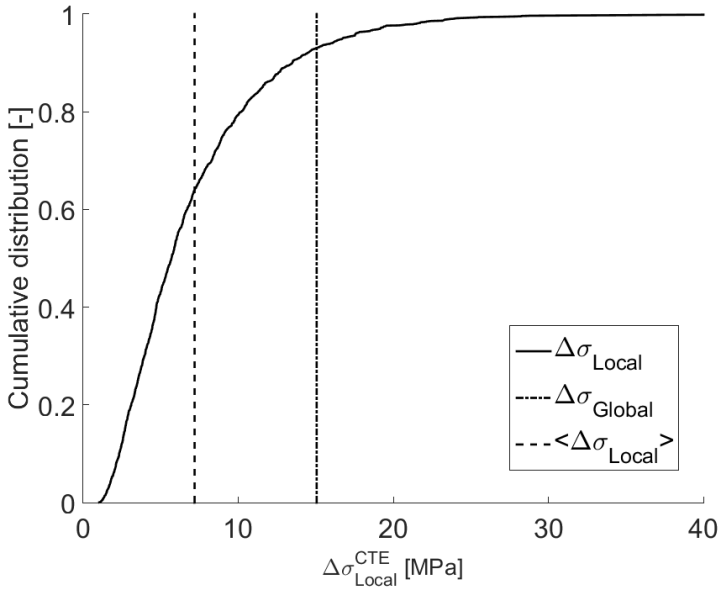

Figure 11: Cumulative distribution of the local contribution $\Delta\sigma_{Local}$ of each particle to the dislocation strengthening caused by thermal mismatch. $<\Delta\sigma_{Local}>$ is the volume-based average strengthening over all the cells of the volume and $\Delta\sigma_{Global}$ is the strengthening computed from global parameters.

5. Conclusions

In the present paper, we performed and exploited multiscale 2D and 3D characterization techniques in association with dedicated modified micromechanical models in order to successfully produce and probe a Magnesium based nanocomposite reinforced by Y_2O_3 particles.

The FSP processing parameters have been successfully optimized by analyzing the particles spatial distribution through 3D tomographic images of several nanocomposites processed with different advancing and rotational speeds of the tool. The *in situ* tensile tests show that the homogeneous incorporation by FSP of a low volume fraction of Y_2O_3 particles (0.33%) inside a Mg matrix increases by 30% the ultimate tensile stress and by 23% the yield strength with an insignificant lost in terms of ductility.

The investigation of the microstructural features (grain size, texture, dislocations and the presence of the particles) reveals that Orowan and CTE mismatch strengthening effects are the main mechanisms responsible of the enhancement of the mechanical properties whereas Hall-Petch strengthening and load transfer effects are negligible. The size and the spatial distribution of the particles inside the matrix have been quantified over four length scales and introduced in dedicated micromechanical hardening models for each mechanisms (Orowan and CTE mismatch). The analyses show that as the spatial distribution of small particles associated with Orowan strengthening is almost random in the present material (P equal 1.22), such strengthening effect can be well described and estimated assuming a random particles distribution. On the opposite, the strengthening effect due to CTE mismatch is overestimated by a factor 2 when using the common approach based on the global volume fraction of particles. Instead, our analysis reveals that better predictions of the enhancement of the mechanical properties are obtained by using the real particle size and spatial distribution extracted from 3D nano-holotomography images.

Acknowledgments

This research has benefited from characterization equipments supported by the Centre of Excellence of Multifunctional Architectured Materials "CEMAM" n° AN-10-LABX-44-01 funded by the Investments for the Future. The authors would like to acknowledge the French's Ministère de l'Enseignement supérieur et

de la Recherche for the financial support. C.M., A.S., F.H. and M.F acknowledge the financial support of the IAP Program from the Belgian State through Belspo, contract IAP7/21 INTEMATE. F.H. acknowledges the financial support of FRIA, Belgium. This research has also been supported (from January 2017) by the European Research Council (ERC) under the European Unions Horizon 2020 research and innovation program (grant agreement n°716678). The authors would like to acknowledge as well the ESRF-MA2584 project, and METSA project (especially F. Mompiou for in-situ TEM experiments).

Data Availability

The raw/processed data required to reproduce these findings cannot be shared at this time due to technical and time limitations.

References

[1] M. Malaki, W. Xu, A. K. Kasar, P. L. Menezes, H. Dieringa, R. S. Varma, and M. Gupta. Advanced metal matrix nanocomposites. Metals, 9(3):330, 2019.

[2] A. Erman, J. Groza, X. Li, H. Choi, and G. Cao. Nanoparticle effects in cast Mg-1% SiC nanocomposites. Mater. Sci. Eng. A., 558:39–43, 2012.

[3] E. Alam, S. Han, Q. B. Nguyen, A. M. S. Hamouda, and M. Gupta. Development of new magnesium based alloys and their nanocomposites. J. Alloys Compd., 509:8522–8529, 2011.

[4] L. Chen, J. Xu, H. Choi, M. Pozuelo, X. Ma, S. Bhowmick, and J. Yang. Processing and properties of magnesium containing a dense uniform dispersion of nanoparticles. Nature, 528:539–543, 2015.

[5] M. Pozuelo, Y. W. Chang, and J. M. Yang. Effect of diamondoids on the microstructure and mechanical behavior of nanostructured Mg-matrix nanocomposites. Mater. Sci. Eng. A., 633:200–208, 2015.

[6] H. Ferkel and B. L. Mordike. Magnesium strengthned by SiC nanoparticles. Mater. Sci. Eng. A., 298:193–199, 2001.

[7] Z. Wang, X. Wang, Y. Zhao, and W. Du. SiC nanoparticles reinforced magnesium matrix composites fabricated by ultrasonic method. Trans. Nonferrous Met. Soc. China, 20:s1029–s1032, 2010.

[8] X. Li, Y. Yang, and X. Chen. Ultrasonic-assisted fabrication of metal matrix nanocomposites. J Mater Sci, 39:3211–3212, 2004.

[9] Y. Chen, Y. B. Guo, M. Gupta, and V. P. W. Shim. Dynamic tensile response of magnesium nanocomposites and the effect of nanoparticles. Mater. Sci. Eng. A., 582:359–367, 2013.

[10] W. W. Leong Eugene and M. Gupta. Simultaneously improving strength and ductility of magnesium using nano-size SiC particulates and microwaves. Adv Eng Mater, 8:735–740, 2006.

[11] A Simar and MN Avettand Fenoel. State of the art about dissimilar metal friction stir welding. Sci Technol Weld Joining, 22(5):389–403, 2017.

[12] R. S. Mishra, P. S. De, and N. Kumar. Friction Stir Welding and Processing, Science and Engineering. Springer, 2014.

[13] Z. Y. Ma, S. R. Sharma, and R. S. Mishra. Microstructural modification of as-cast Al-Si-Mg alloy by friction stir processing. Metall Mater Trans A, 37:3323–3336, 2006.

[14] H. Eskandari and R. Taheri. A novel technique for development of aluminum alloy matrix/tib2/al2o3 hybrid surface nanocomposite by friction stir processing. Proc Mater Sci, 11:503–508, 2015.

[15] Y. Morisada, H. Fujii, T. Nagaoka, and M. Fukusumi. Effect of friction stir processing with SiC particles on microstructure and hardness of AZ31. Mater Sci Eng A, 433:50–54, 2006.

[16] P. Asadi, G. Faraji, A. Masoumi, and M. K. B. Givi. Experimental investigation of magnesium-base nanocomposite produced by friction stir processing: effects of particle types and number of friction stir processing passes. Metall Mater Trans A, 42:2820–2832, 2011.

[17] C. J. Lee, J. C. Huang, and P. J. Hsieh. Mg based nano-composites fabricated by friction stir processing. Scripta Mater, 54:1415–1420, 2006.

[18] G. Faraji and P. Asadi. Characterization of AZ91/alumina nanocomposite produced by FSP. Mater. Sci. Eng. A., 528:2431–2440, 2011.

[19] A. Mertens, A. Simar, J. Adrien, E. Maire, H.-M. Montrieux, F. Delannay, and J. Lecomte-Beckers. Influence of fibre distribution and grain size on the mechanical behavior of friction stir processed Mg-C composites. Mater Charact, 107:125–133, 2015.

[20] A.M. Redsten, E.M. Klier, A.M. Brown, and D.C. Dunand. Mechanical properties and microstructure of cast oxide-dispersion-strengthened aluminum. Mater Sci Eng A, 201(1):88 – 102, 1995.

[21] S. Terzi, R. Daudin, J. Villanova, P. Srirangam, P. Lhuissier, L. Salvo, E. Boller, R. Schweins, P. Lindner, JJ. Blandin, P. Lee, and H. Lemmel. X-Ray Tomography and Small-Angle Neutron Scattering Characterization of Nano-Composites: Static and In Situ Experiments, pages 1389–1393. Springer International Publishing, 2016.

[22] W. B. Lievers and A. K. Pilkey. Matrix-erosion tessellation: comparing particle clustering measures extracted from three-dimensional vs two-dimensional images. Metall Mater Trans A, 40A:36–45, 2009.

[23] A. de Vaucorbeil, C.W. Sinclair, and W.J. Poole. Dislocation glide through non-randomly distributed point obstacles. Phil Mag, 93(27):3664–3679, 2013.

[24] M. Avettand, A. Simar, R. Shabadi, R. Taillard, and B. de Meester. Characterization of oxide disperion strengthened copper based materials developed by friction stir processing. Mater Design, 60:343–357, 2014.

[25] R. Daudin, S. Terzi, C. Mallmann, R. Sanchez Martin, P. Lhuissier, and E. Boller. Indirect improvement of high temperature mechanical properties of mg-based alloy elektron21 by addition of aln nanoparticles. Mater Sci Eng A, 688:76–82, 2017.

[26] C. Jonckheere, B. de Meester, A. Denquin, and A. Simar. Torque, temperature and hardening precipitation evolution in dissimilar friction stir welds between 6061-T6 and 2014-T6 aluminum alloys. J. Mater. Process. Technol., 213:826–837, 2013.

[27] S. Askari, S. Silling, B. London, and M. Mahoney. Modeling and analysis of friction stir welding processes. Friction stir welding and processing IV, pages 43–54, 2001.

[28] D. Khayyamin, A. Mostafapour, and R. Keshmiri. The effect of process parameters on microstructural characteristics of AZ91/SiO_2 composite fabricated by FSP. Mater Sci Eng A, 559:217–221, 2013.

[29] A. Shamsipur, S. F. Kashani-Bozorg, and A. Zarei-Hanzaki. The effects of friction-stir process parameters on the fabrication of Ti/SiC nano-composite surfaces. Surf. Coat. Technol., 206:1372–1381, 2011.

[30] M. Langer, A. Pacureanu, H. Suhonen, Q. Grimal, P. Cloetens, and F. Peyrin. X-Ray nanotomography resolves the 3D human bone ultrastructure. Plos One, 7(8):1–7, 2012.

[31] K. V. Jata and S. L. Semiatin. Continuous dynamic recrystallization during friction stir processing of high strength aluminum alloys. Scr. Mater, 43:743–749, 2000.

[32] P. L. Threadgill. Friction stir welding - the state of the art. TWI Report 678, 1999.

[33] P. Asadi, M. K. Besharati Givi, K. Abrinia, M. Taherishargh, and R. Salekrostam. Effects of SiC particle size and process parameters on the microstructure and hardness of AZ91/SiC composite layer fabricated by FSP. J Mater Eng Perform, 20:1554–1562, 2011.

[34] M. Najafi, A. M. Nasiri, and A. H. Kokabi. Microstructure and hardness of friction stir processed AZ31 with SiC_p. Int. J. Mod Phys B, 22:2879–2885, 2008.

[35] W. B. Lee, Y. M. Yeon, and S. B. Jung. Joint properties of friction stir welded az31b h24 magnesium alloy. Mater Sci Techno, 19:785–790, 2003.

[36] M. M. Attallah and H. G. Salem. Friction stir welding parameters: a tool for controlling abnormal grain growth during subsequent heat treatment. Mater. Sci. Eng. A., 391:51–59, 2005.

[37] W. A. Spitzig, J. F. Kelly, and O. Richmond. Quantitative characterization of second-phase populations. Metallography, 18:235–261, 1985.

[38] S. Ghosh. Micromechanical Analysis and Multi-Scale Modeling Using the Voronoi Cell Finite Element Method. Computational Mechanics and Applied Analysis. CRC Press, 2011.

[39] J.P Anson and J.E Gruzleski. The quantitative discrimination between shrinkage and gas microporosity in cast aluminum alloys using spatial data analysis. Mater Charact, 43(5):319 – 335, 1999.

[40] J. Boselli, P. D. Pitcher, P. J. Gregson, and I. Sinclair. Secondary phase distribution analysis via finite body tessellation. J Microscopy, 195:104–112, 1999.

[41] F. Hannard, S. Castin, E. Maire, R. Mokso, T. Pardoen, and A. Simar. Ductilization of aluminium alloy 6056 by friction stir processing. Acta Mater, 130:121 – 136, 2017.

[42] A.E. Scott, I. Sinclair, S.M. Spearing, M.N. Mavrogordato, and W. Hepples. Influence of voids on damage mechanisms in carbon/epoxy composites determined via high resolution computed tomography. Comp Sci Technol, 90:147 – 153, 2014.

[43] F. Hannard, T. Pardoen, E. Maire, C. Le Bourlot, R. Mokso, and A. Simar. Characterization and micromechanical modelling of microstructural heterogeneity effects on ductile fracture of 6xxx aluminium alloys. Acta Mater, 103:558–572, 2016.

[44] S. F. Hassan and M. Gupta. Development and characterization of ductile Mg/Y_2o_3 nanocomposites. Trans ASME, 129:462–467, 2007.

[45] S. F. Hassan. Effect of primary processing techniques on the microstructure and mechanical properties of nano-Y_2O_3 reinforced magnesium nanocomposites. Mater Sci Eng A, 528:5484–5490, 2011.

[46] G. Bhargava, W. Yuan, S. S. Webb, and R. S. Mishra. Influence of texture on mechanical behavior of Friction-Stir-Processed magnesium alloy. Metall Mater Trans A, 41A:13–17, 2010.

[47] H. Kokawa, Y. S. Sato, and S. Mironov. Texture development during friction stir welding of magnesium alloys. Mater Sci Forum, 702-703:43–47, 2012.

[48] R. Casati and M. Vedani. Metal matrix composites reinforced by nano-particles - a review. Metals, 4:65–83, 2014.

[49] N. Ramakrishnan. An analytical study on strengthening of particulate reinforced metal matrix composites. Acta Mater, 44(1):69–77, 1996.

[50] S. C. Tjong. Novel nanoparticle-reinforced metal matrix composites with enhanced mechanical properties. Adv Eng Mater, 9(8):639–652, 2007.

[51] N. Stanford and M. R. Barnett. Effect of particles on the formation of deformation twins in a magnesium-based alloy. Mater Sci Eng A, 2009.

[52] C. Mallmann, A. Simar, E. Ferrié, M. Fivel, and E. T. Lilleodden. Influence of Y_2O_3 nanoparticles on the twinning of single crystalline magnesium. Scr. Mater, 138:79–82, 2017.

[53] MATLAB. version 8.5.0.197613 (R2015a). The MathWorks Inc., Natick, Massachusetts, 2015.

[54] A. J. E. Foreman and M. J. Makin. Dislocation movement through random arrays of obstacles. Can. J. Phys., 45(2):511–517, 1967.

[55] A. Sanaty-Zadeh. Comparison between current models for the strength of particulate-reinforced metal matrix nanocomposites with emphasis on consideration of Hall-Petch effect. Mater. Sci. Eng. A., 531:112–118, 2012.

[56] D. Hull and D. J. Bacon. Introduction to dislocations. Elsevier, fifth edition edition, 2011.

[57] R. J. Arsenault and N. Shi. Dislocation generation due to differences between the coefficient of thermal expansion. Mater. Sci. Eng., 81:175–187, 1986.

[58] L. Commin, M. Dumont, J-E Masse, and L. Barrelier. Friction stir welding of az31 magnesium alloy rolled sheets : Influence of processing parameters. Acta Mater, 57:326–334, 2009.

[59] M. F. Ashby. Work hardening of dispersion-hardened crystals. Phil Mag, 14(132):1157–1178, 1966.

[60] D. C. Dunand and A. Mortensen. On plastic relaxation of thermal stresses in reinforced metals. Acta metall. mater., 39(2):127–139, 1991.